Petroleum Science 23 (2026) 190–204

Contents lists available at ScienceDirect

Petroleum Science

journal homepage: www.keaipublishing.com/en/journals/petroleum-science

Original Paper

Fast beam migration capable of dealing with intersecting events

Zhi-Miao Chang [a], Fu-Xing Han [a], Zheng-Hui Gao [a,*], Zhang-Qing Sun [a], Shou-Dong Huo [b], Gang Li [c,d], Ming Zhang [e]

[a] State Key Laboratory of Deep Earth Exploration and Imaging, College of Geoexploration Science and Technology, Jilin University, Changchun, 130026, Jilin, China
[b] Key Laboratory of Petroleum Resources Research, Institute of Geology and Geophysics, Chinese Academy of Science, Beijing, 100029, China
[c] Jinan Railway Transportation Group Co, Ltd., Jinan, 250014, Shandong, China
[d] Shandong Jiaotong University, Jinan, 250357, Shandong, China
[e] Daqing Branch, China National Logging Corporation, Daqing, 163412, Heilongjiang, China

ARTICLE INFO

Article history:
Received 26 April 2025
Received in revised form
11 August 2025
Accepted 24 October 2025
Available online 28 October 2025

Edited by Meng-Jiao Zhou

Keywords:
Fast beam migration (FBM)
Intersecting events
Multimodal optimization method
Neighborhood crowding differential evolution (NCDE) algorithm
High-dimensional computing problem

ABSTRACT

Fast beam migration (FBM), characterized by its super-high efficiency in velocity model building, consists of three main steps: beam forming, beam propagation, and image forming. The super-high efficiency is achieved by beam forming, as it needs only to be performed once for one dataset and is independent of velocity, and the other two steps take relatively little time. However, compared to the beam-propagation and image-forming steps, the beam-forming step is still quite time-consuming owing to the high-dimensional computing problem of estimating the source and receiver slope orientation of a beam. Furthermore, previous methods for estimating the source and receiver slope orientation of a beam struggled to deal with intersecting events, leading to poor imaging results for complex subsurface structures, such as unconformities or faults, where events often intersect. We propose the use of a three-step multimodal optimization method based on the neighborhood crowding differential evolution (NCDE) algorithm to estimate the source and receiver slope orientation of a beam during the beam-forming step, which can quickly and accurately obtain slope orientations when events intersect. We first test the three-step multimodal optimization algorithm on a 3D super-gather and provide the parameter criteria. We then apply the FBM based on the three-step multimodal optimization algorithm to the Marmousi 2 and 3D SEG/EAGE salt models. Both results demonstrate that the proposed method can image intersecting events well and that the imaging quality of complex zones is improved. We also apply the proposed method to a 2D offshore seismic dataset containing abundant intersecting events, which validates the practicality of the proposed method.

1. Introduction

Seismic migration is a key technique for velocity model building and structural imaging. To achieve an appropriate velocity model, the migration process is performed iteratively, which implies that faster migration allows for more iterations. Thus, accelerating this process is critical for reducing the turnaround time required to build a velocity model. Owing to the increasing complexity of exploration targets, broadband, wide-azimuth, and high-density exploration technology has been widely used to acquire high-quality seismic information (Wang, 2019; Su et al., 2021). However, the consequent dramatic increase in the amount of seismic data poses a significant challenge to the migration procedure (datasets are typically hundreds to thousands of terabytes in size). In addition, in special cases, including salt boundary interpretation (Wang et al., 2008; Leveille et al., 2011; Wu et al., 2018) and seismic while drilling (Esmersoy et al., 2005; Yang and Peng, 2018), the velocity model must be updated and imaged in real time. Therefore, fast and accurate migration methods remain a focus of research.

Currently, reverse time migration and Kirchhoff migration each account for nearly half of the market, whereas beam migration and one-way wave-equation migration generally only play auxiliary roles. Theoretically, reverse time migration is an ideal imaging technique. However, because the efficiency of generating imaging

* Corresponding author.
E-mail address: gaozh2020@jlu.edu.cn (Z.-H. Gao).
Peer review under the responsibility of China University of Petroleum (Beijing).

https://doi.org/10.1016/j.petsci.2025.10.024

gathers from reverse time migration has not been completely solved, Kirchhoff migration continues to be the most popular migration method in the industry (Zhang, 2018). In the standard Kirchhoff migration, the amplitude on one trace is spread across the entire image volume along an isochronous surface. Thus, the computational cost of the standard Kirchhoff migration is proportional to the amount of input data and the size of the model (or the migration aperture), and remains excessive for large surveys or interactive processing (including salt boundary interpretation and seismic while drilling). To address this problem, several input-steering implementations of Kirchhoff migration, including parsimonious Kirchhoff migration (Hua and McMechan, 2003, 2009), wavepath migration (Sun and Schuster, 2001), and Kirchhoff beam migration (Sun et al., 2000a, 2000b), have been developed using the slope information of local seismic event. For both parsimonious Kirchhoff migration and wavepath migration, the slope information estimated using the local slant stack is used to limit the migration aperture to the first Fresnel zone portion of the isochronous surface. For parsimonious Kirchhoff migration, the traveltime calculation is embedded in the migration procedure and there is no need to calculate the traveltime table before migration (Hua and McMechan, 2003). However, for wavepath migration, a traveltime table is still required. Furthermore, for parsimonious Kirchhoff migration, input data is decimated by applying a threshold value and keeping only peak and trough values, and for wavepath migration, every n-th trace is slant-stacked and migrated. For Kirchhoff beam migration, improved efficiency is achieved by applying local slant stack in the super-gather and migrating one super-gather at a time (Sun et al., 2000a, 2000b; Fomel and Tanushev, 2009; Hu et al., 2015). All these methods remain traditional Kirchhoff-type methods, and the imaging results are still affected by the infamous multi-pathing problem which is common in complex velocity models.

Based on the above input-steering ideas, and combined with the classic Gaussian beam migration (GBM) theory which can overcome the multi-pathing problem (Hill, 1990, 2001), an ultra-efficient and accurate imaging algorithm called fast beam migration (FBM) was developed (Gao et al., 2006; Gao and Zhang, 2007). First, a speedup for FBM is obtained by decomposing the input data into a set of beams which are seismic events characterized by arrival time, source and receiver location, amplitude, and source and receiver slope orientation (Tanushev et al., 2017). An additional speedup is then achieved by spreading the beam over a small patch near the beam imaging point using the beam's information, especially source and receiver slope orientation. In addition, owing to the complex-valued traveltime of Gaussian beam, the multi-pathing problem can be solved effectively.

FBM consists of three main steps – beam forming, beam propagation, and image forming. Accurate beam forming is a prerequisite for beams to propagate and image exactly, and plays a decisive role for the final imaging quality. The estimation of the source and receiver slope orientation of a beam is a key point in the beam-forming step, and directly restricts the accuracy of beam forming. Currently, there are three main methods for calculating source and receiver slope orientation. The first method simultaneously applies the local slant stack in multiple types of conventional gathers (common shot gather, common receiver gather, and common offset gather) (Gao et al., 2006; Gao and Zhang, 2007). The second method uses a multidimensional slant stack in a super-gather (Masters and Sherwood, 2005; Sherwood et al., 2008, 2009). The last method employs a plane wave destructor in a super-gather (Popovici et al., 2013a, b). For datasets from complex subsurface structures such as unconformities or faults, phenomena in which events intersect are quite common. Because of the influence of large spatial sampling along the crossline direction and the phenomenon of event intersection, the first method is both time-consuming and challenging for 3D case (Gao and Zhang, 2007; Wang et al., 2008). The second method requires uniform sampling along four directions (p_{sx}, p_{sy}, p_{rx}, and p_{ry}) for 3D case (if the number of sampling points along each direction is set to 100, 10^8 calculations of slant stack are required), which will cause serious high-dimensional computing problem, and at the same time, this method lacks the ability to deal with intersecting events. The third method is theoretically difficult to deal with intersecting events (Fomel, 2002), and also needs to face the high-dimensional computing problem. Consequently, problems remain in estimating source and receiver slope orientation of a beam for the FBM, especially when events intersect.

Based on the multimodality of the coherency of intersecting events shown along the directions of different slopes, Gao et al. (2019) first transformed the estimation of slopes for intersecting events into a typical multimodal optimization problem (Das et al., 2011) in the field of intelligent optimization and proposed the use of a niching method called the neighborhood-based crowding differential evolution (NCDE) algorithm (Qu et al., 2012) to capture the local slopes simultaneously. Gao et al. (2022) proposed a novel three-step multimodal optimization method based on the NCDE algorithm that can efficiently and accurately obtain the local slopes of intersecting events. The so-called multimodal optimization problem refers to an optimization problem that aims to find multiple global and local optima rather than just a single optimum. This is exactly the same as our goal of finding the local slopes of intersecting events (we intend to obtain not only global optima but also high-quality local optima corresponding to the desired slopes). Solving multimodal optimization problems is an important research topic in the field of intelligent optimization. In this field, people usually refer to optimization methods specifically designed to solve multimodal optimization problems as niching methods. Conventional intelligent optimization methods, including the genetic algorithm (Holland, 1992), particle swarm optimization algorithm (Kennedy and Eberhart, 1995), and differential evolution (DE) algorithm (Price et al., 2006), can only obtain one global optimum when dealing with multimodal optimization problems. However, niching methods enable a conventional intelligent optimization algorithm to properly search over multimodal fitness landscapes by driving subsets of a population toward different areas and promoting distributed convergence to multiple peaks simultaneously in a single run (Das et al., 2011).

The original NCDE algorithm proposed by Qu et al. (2012) was developed based on the conventional DE algorithm (Price et al., 2006). By introducing a neighborhood mutation strategy into the DE algorithm, the NCDE algorithm can keep the multiple optima discovered during the evolution process and evolve toward the respective local optima. However, when fully adopting the NCDE algorithm (Gao et al., 2019, 2022), to obtain a robust and high-precision estimation of the source and receiver slope orientations for intersecting events, a fine search is required, which results in more function calls and heavy computational cost. Furthermore, this problem will be enhanced because of the intrinsic randomness of the NCDE algorithm. To address this problem, the three-step multimodal optimization method proposed by Gao et al. (2022) cascades the NCDE algorithm with the hill-valley detection algorithm (Ursem, 1999) and the Nelder-Mead simplex algorithm (Nelder and Mead, 1965). Thus, the requirement for a fine search when the NCDE algorithm is fully adopted can be avoided. Gao et al. (2022) also provided the setting criteria of parameters for both 2D and 3D conditions and verified the high precision and efficiency of the method through numerical analysis of both 2D and 3D conventional synthetic gathers. They integrated this method into a dip-steering median filter (Huo et al., 2017) and

achieved excellent filtering results in noisy and complex wavefields with signal-to-noise ratios as low as 15 dB. Thus, the three-step multimodal optimization method can be used to estimate the source and receiver slope orientation of a beam during the beam-forming step. In addition, as an intelligent optimization algorithm, it is not very sensitive to the dimensions of the problem (Xie and Gajewski, 2017) and can be used to solve the high-dimensional computing problem corresponding to 3D super-gather.

This study proposes a new FBM implementation using a the three-step multimodal optimization method based on the NCDE algorithm. This implementation can deal with intersecting events and overcome the high-dimensional computational problem when estimating the source and receiver slope orientation of a beam in a 3D super-gather. High-quality imaging results can be obtained for complex subsurface structures. First, we briefly describe the theories of the FBM and three-step multimodal optimization method. Subsequently, the optimization method is tested on a 3D super-gather and the parameter criteria are determined. Next, we apply the FBM based on the three-step multimodal optimization method to the Marmousi 2 and 3D SEG/EAGE salt models, where the phenomena in which events intersect are very common. Finally, a 2D offshore seismic dataset containing abundant intersecting events is used to evaluate its practicality.

2. Theory

2.1. Fast beam migration (FBM)

FBM mainly comprises three steps: beam forming, beam propagation, and image forming (Fig. 1), and it is typically performed in a super-gather. A super-gather is a set of traces whose sources and receivers are located in the vicinity of the reference points (Fig. 2) (Sun et al., 2000a, 2000b). Because the coordinates of the source and receiver location in the super-gather are both variable, we can estimate the source and receiver slope orientation of a beam simultaneously. It is much easier to carry out the beam-forming step in a super-gather than in multiple types of conventional gathers. Thus, performing the beam-forming step in the super-gather is preferred. In the beam-forming step, the goal is to decompose the seismic data into beams along different slope orientations. When estimating the source and receiver slope orientation of a beam in a super-gather, especially for 3D

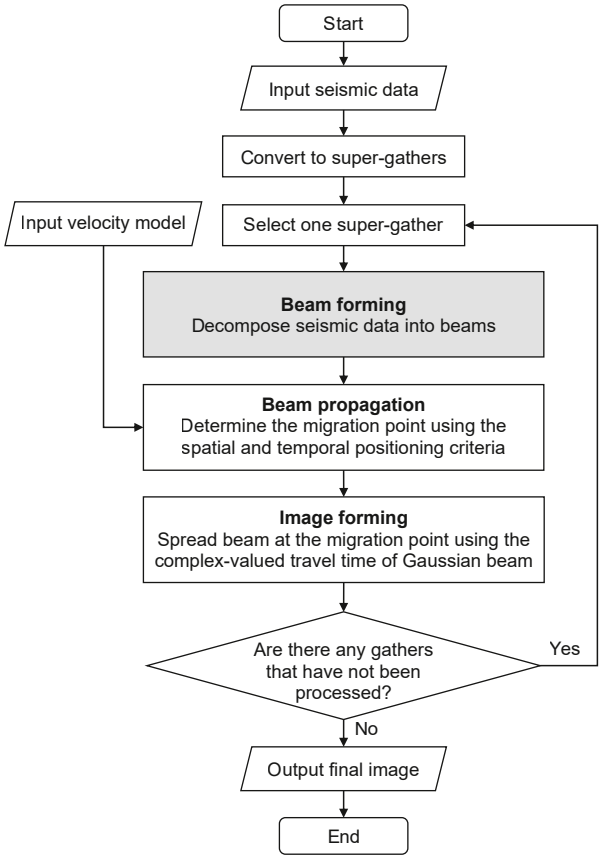

Fig. 1. Workflow of the conventional FBM.

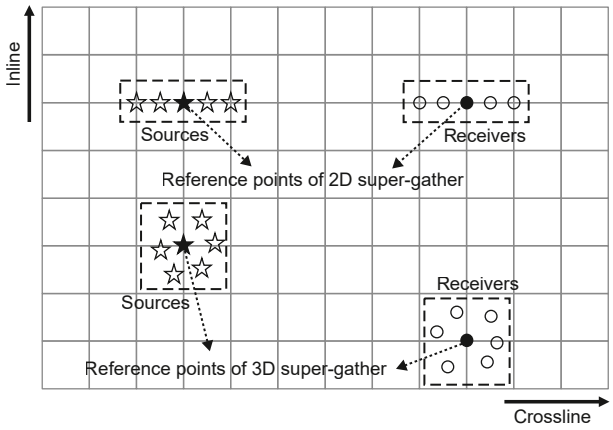

Fig. 2. Schematic diagram of 2D and 3D super-gathers.

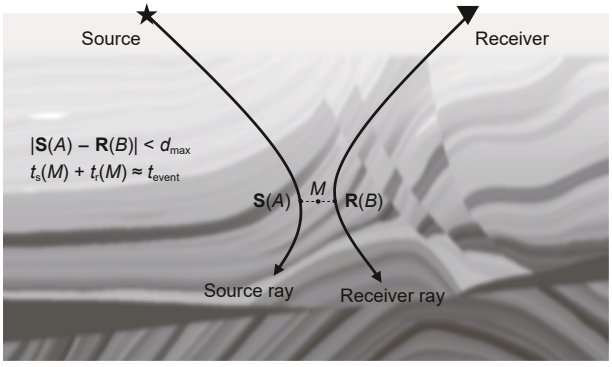

Fig. 3. Schematic diagram of beam propagation.

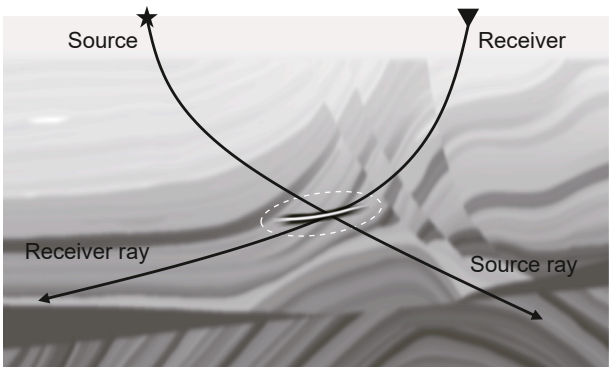

Fig. 4. Schematic diagram of image forming.

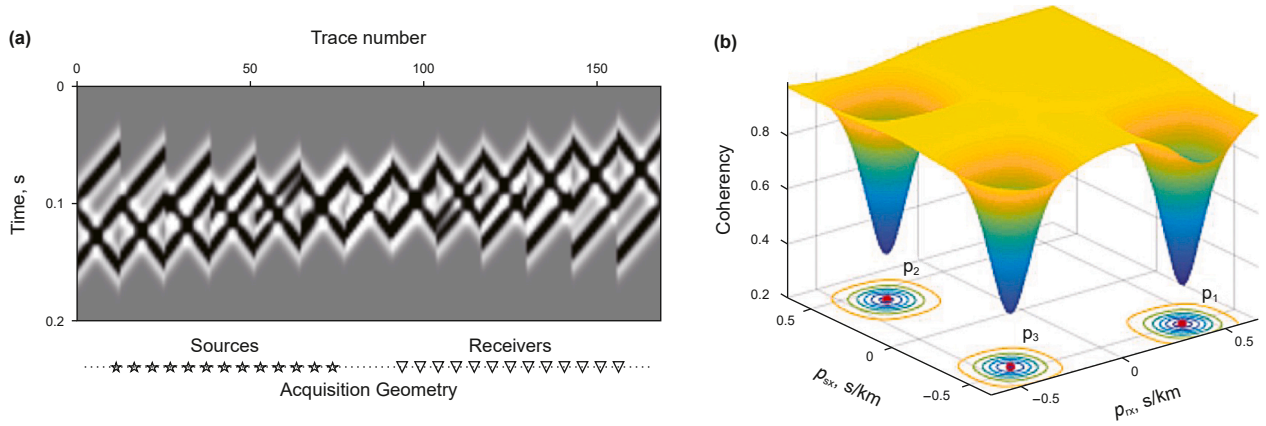

Fig. 5. **(a)** 2D super-gather with three intersecting events with different source and receiver slope orientations (−0.50 s/km, 0.40 s/km) [p_1], (0.40 s/km, −0.35 s/km) [p_2], and (−0.45 s/km, −0.40 s/km) [p_3] and **(b)** coherency results obtained at the intersection location along different slope orientations according to the variance-based coherency formula.

Table 1
Core steps of the three-step multimodal optimization method based on the NCDE algorithm for processing an individual super-gather.

Step 1) Select one super-gather.
Step 2) Pick the arrival times of local seismic events according to their respective energy.
Step 3) For each arrival time
Step 3.1) Execute the NCDE algorithm to make *NP* individuals evolve toward their respective local optima (coherency extrema corresponding to the slope orientations).
Step 3.2) Perform niche detection by the hill-valley detection algorithm, retaining one excellent individual in each valley.
Step 3.3) Apply the Nelder-Mead simplex algorithm to converge the selected excellent solution in each valley to the local extremum.
Step 3.4) Stack along the respective slope orientations to obtain the beams.
Step 3.5) Save the information of each beam, including arrival time, source and receiver location, amplitude, and source and receiver slope orientation.
End for

condition, previous methods (Masters and Sherwood, 2005; Sherwood et al., 2008, 2009; Popovici et al., 2013a, 2013b) mainly faced two challenges: how to deal with intersecting events, and the high-dimensional computing problem. To address these two challenges, we propose the use of a high-precision and efficient three-step multimodal optimization method based on the NCDE algorithm to estimate the slope orientation of a beam, which will be presented in the next subsection. Once the slope orientations of the beams are obtained, the seismic data can be decomposed into beams through stacking along the respective slope orientations.

In the beam-propagation step, the estimated source and receiver slope orientation of the beam is used as the initial direction for ray tracing. Ray tracing can then be performed in a medium from the source and receiver positions. Finally, the migration position can be determined using the spatial and temporal positioning criteria (Fig. 3). The spatial positioning criterion is as follows:

$$|\mathbf{S}(A) - \mathbf{R}(B)| < d_{\max} \tag{1}$$

where $\mathbf{S}(A)$ and $\mathbf{R}(B)$ represent points on the source and receiver rays, respectively, and $d_{\max}$ represents the maximum correlation distance (when the nearest distance between $\mathbf{S}(A)$ and $\mathbf{R}(B)$ is beyond this threshold, the corresponding beam is considered

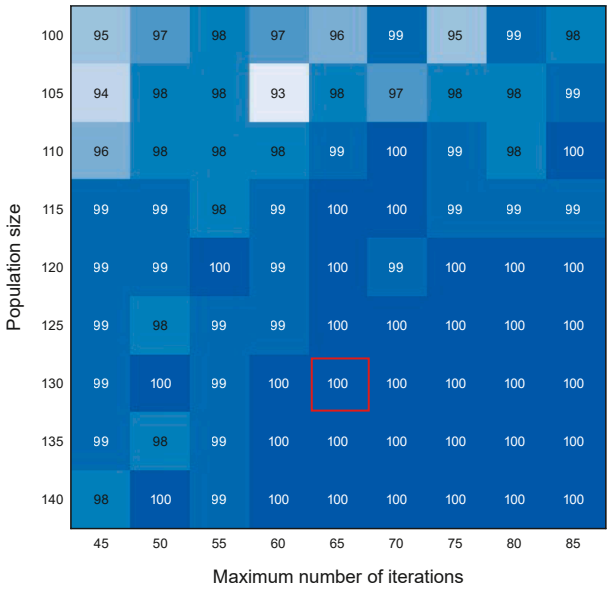

Fig. 6. The statistical results of 100 independent runs for each combination in which at least one individual moves into each valley using the NCDE algorithm for the 3D super-gather.

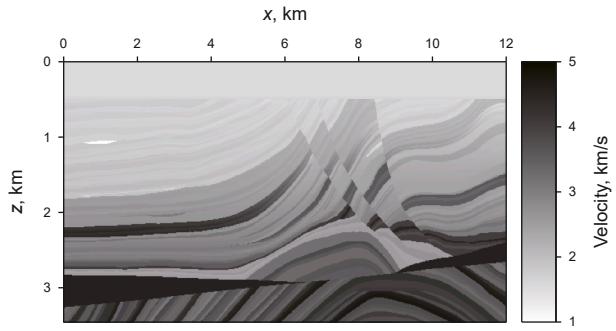

Fig. 7. Velocity profile of the Marmousi 2 model.

uncorrelated and discarded). The temporal positioning criterion is as follows:

$$t_s(M) + t_r(M) \approx t_{event} \quad (2)$$

where M represents the migration position of a beam, $t_s(M)$ and $t_r(M)$ represent the arrival time from the source and receiver, respectively, and t_{event} is the arrival time of the beam. To determine the migration position of a beam means to find the point whose arrival time is closest to the beam's arrival time in the vicinity of the two rays' nearest area that satisfies Eq. (1).

In the image-forming step, the beam is spread out at the migration point according to the complex-valued traveltimes of Gaussian beams from the source and receiver positions. First, the real part of the sum of the traveltimes is used to obtain the imaging amplitude. The imaginary part of the sum of the traveltimes is then used to apply proper attenuation to the amplitude (Fig. 4).

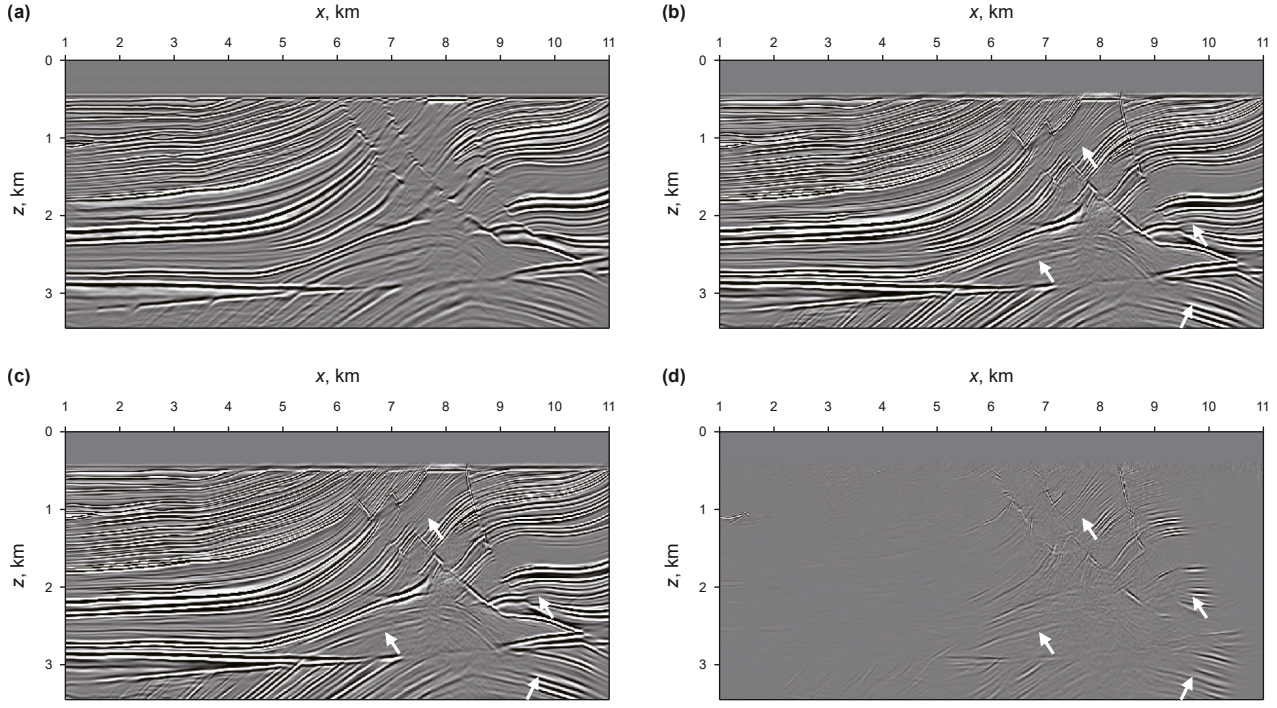

Fig. 8. Migration results of the Marmousi 2 model: **(a)** GBM, **(b)** NCDE-based FBM when at most three intersecting events are considered, **(c)** DE-based FBM, and **(d)** difference between **(b)** and **(c)**.

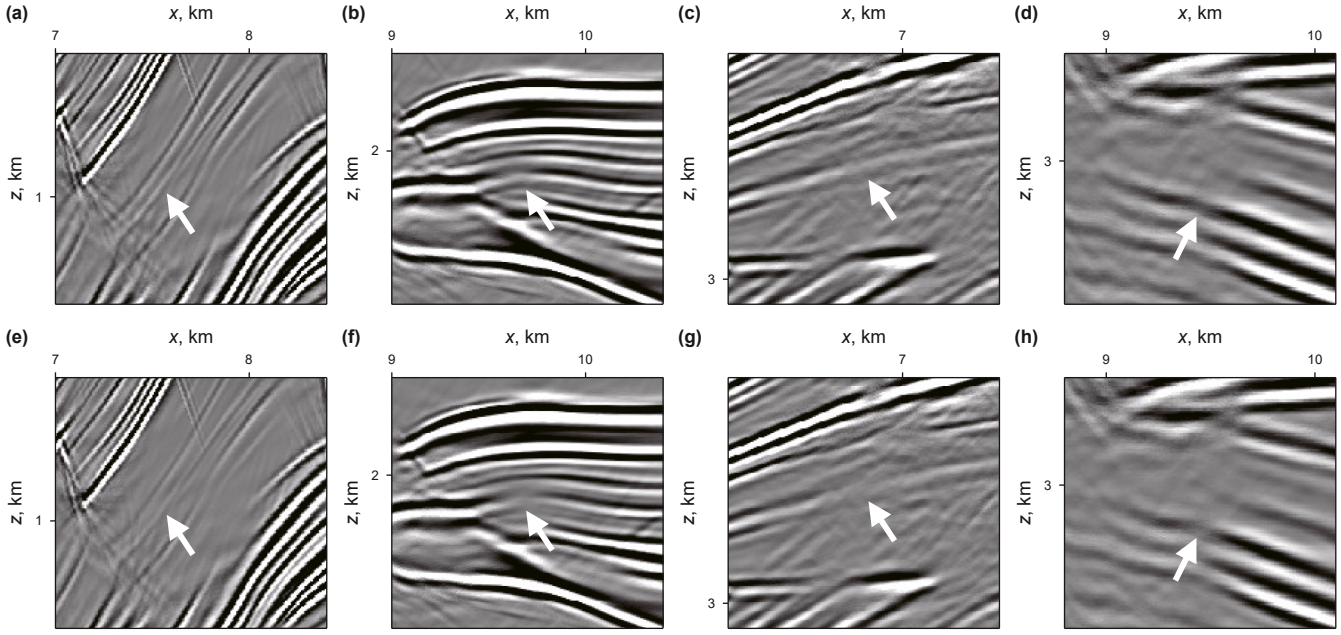

Fig. 9. Magnified views of the migration results of the Marmousi 2 model: **(a)**, **(b)**, **(c)**, and **(d)** are for the result of NCDE-base FBM, and **(e)**, **(f)**, **(g)**, and **(h)** are for that of DE-based FBM.

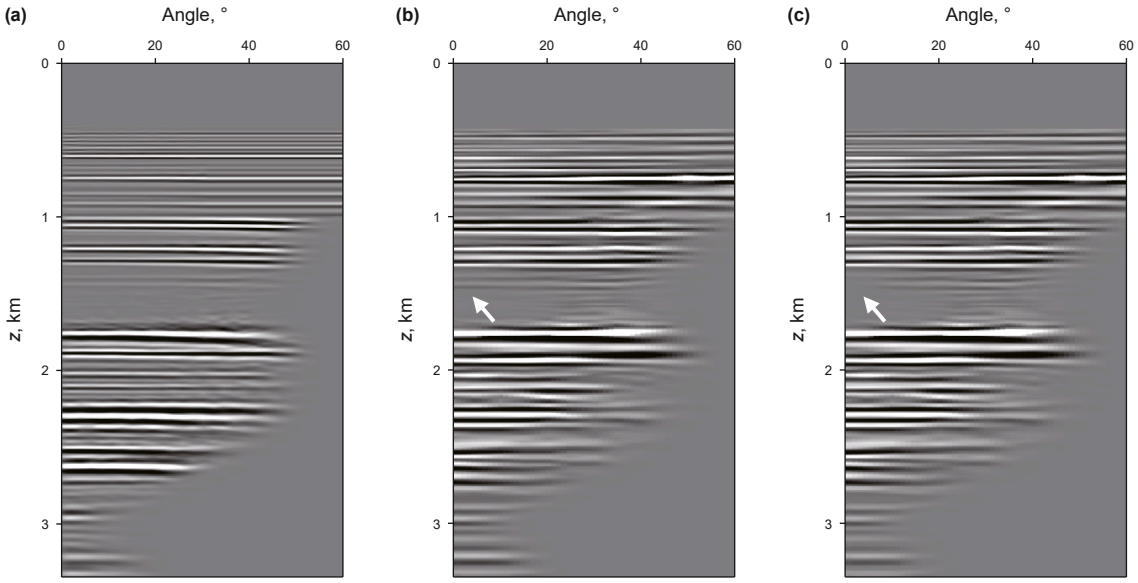

Fig. 10. ADCIGs of the Marmousi 2 model extracted at $x = 10.3$ km: **(a)** GBM, **(b)** NCDE-based FBM when at most three intersecting events are considered, and **(c)** DE-based FBM.

Table 2
Comparison of the running times of NCDE-based FBM and GBM for the Marmousi 2 model.

Migration methods	Running time, min
NCDE-based FBM	4.35
NCDE-based FBM (just record the beam-propagation and image-forming steps)	1.46
GBM	78.40

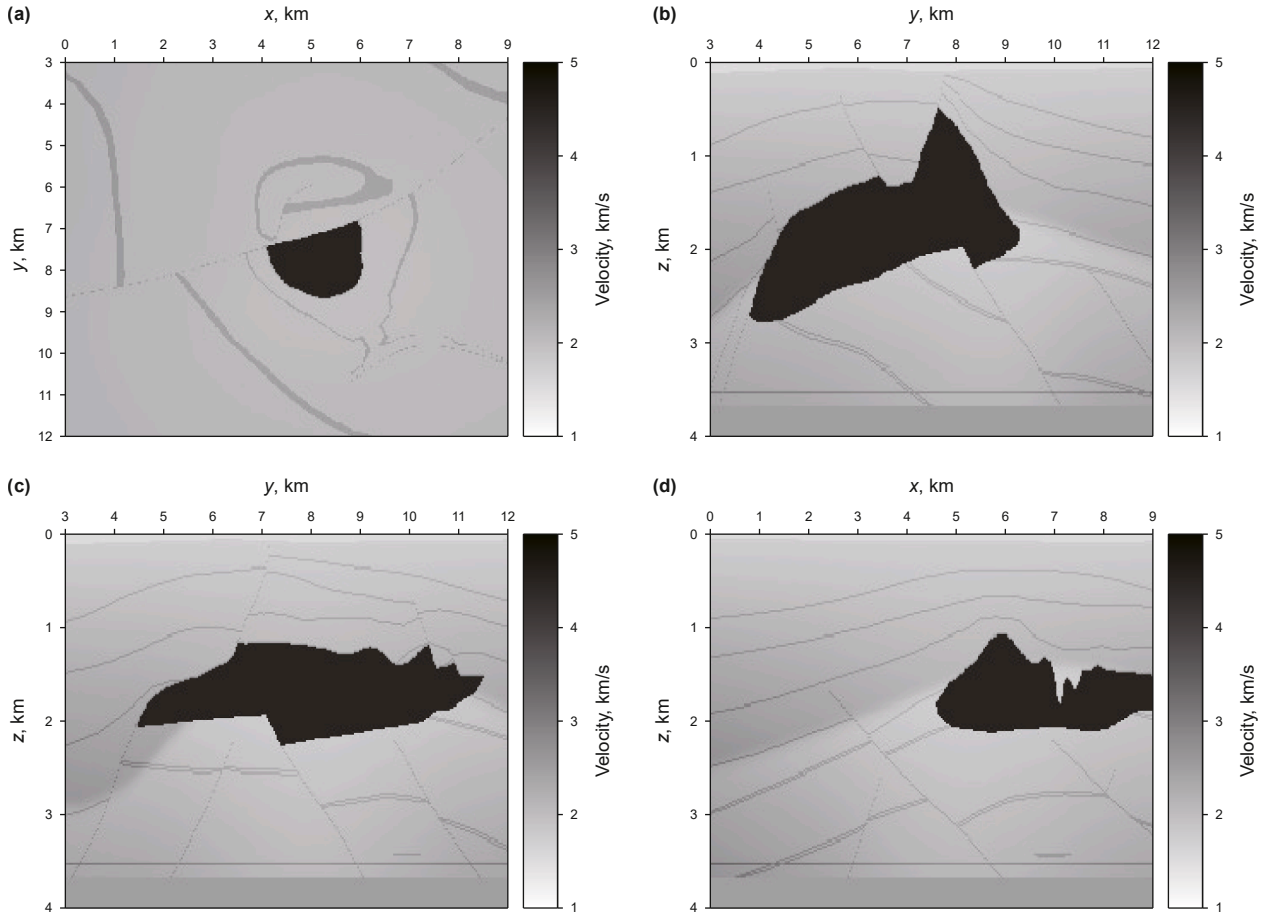

Fig. 11. Velocity profiles of the 3D SEG/EAGE salt model at different locations: **(a)** $z = 1020$ m, **(b)** $x = 4620$ m, **(c)** $x = 6260$ m, and **(d)** $y = 6280$ m.

2.2. NCDE-based three-step multimodal optimization algorithm

Coherency is a measure of the similarity between waveforms (Chopra and Marfurt, 2007). When coherency is calculated along the source and receiver slope orientation of a beam in the super-gather, an extremum is obtained. When events intersect, several extrema corresponding to the slope orientations respectively will be generated.

Fig. 5(a) shows a 2D super-gather with 13 sources and 13 receivers. There are three events intersecting at 0.1 s with source and receiver slope orientations of (−0.50 s/km, 0.40 s/km) [p_1], (0.40 s/km, −0.35 s/km) [p_2], and (−0.45 s/km, −0.40 s/km) [p_3]. Fig. 5(b) shows the coherency surface calculated at the intersecting location according to the variance-based coherency formula (Chopra and Marfurt, 2007). The three slope orientations correspond accurately to the three extrema. Thus, when events intersect, the estimation of the slope orientation of a beam can be transformed into a multimodal optimization problem.

Gao et al. (2019) first proposed the use of the NCDE algorithm to simultaneously capture the source and receiver slope orientations of intersecting events. The NCDE algorithm introduces a neighborhood mutation strategy into the conventional population-based heuristic DE algorithm to keep the multiple optima discovered during the evolution process and evolve toward the respective local optima. The conventional DE algorithm generates new individuals based on the differences among different individuals within a population. Compared with the original DE algorithm, only the neighborhood size m is introduced to control the number of individuals selected in each subset (Qu et al., 2012). Notably, when the parameter m equals the population size NP, the NCDE algorithm degenerates into the standard DE algorithm, losing its multimodal optimization capability and converging to only a single global optimum.

Gao et al. (2022) proposed a three-step multimodal optimization method that cascades the NCDE algorithm with the hill-valley detection algorithm (Ursem, 1999) and the Nelder-Mead simplex algorithm (Nelder and Mead, 1965) to avoid the need for a fine search when fully adopting the NCDE algorithm. The hill-valley detection algorithm is a niche detection algorithm that can determine whether two points belong to a niche by setting interior points. This algorithm can be used to select one excellent solution in each valley. The Nelder-Mead simplex algorithm is a popular

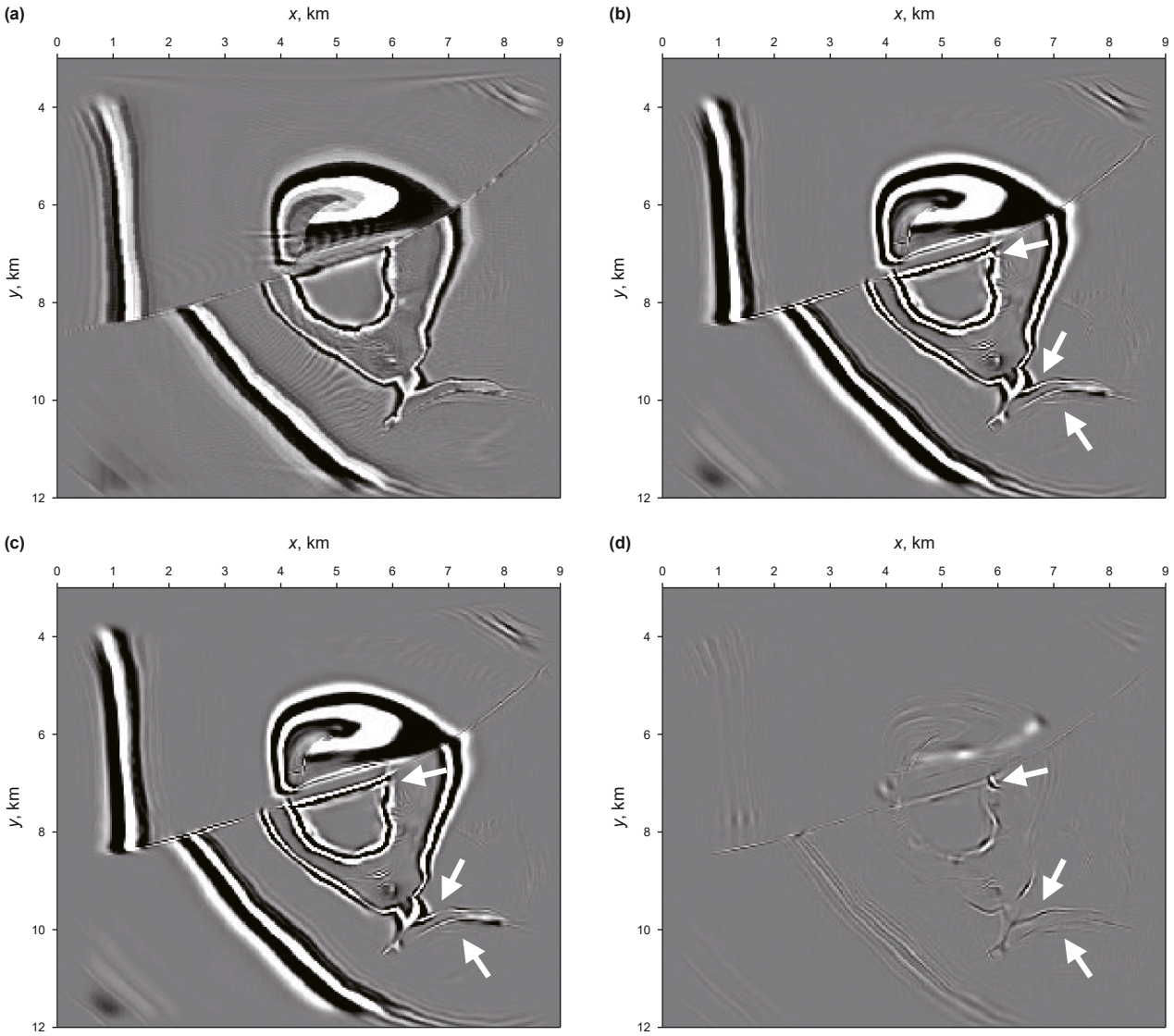

Fig. 12. Migration results of the 3D SEG/EAGE salt model at $z = 1020$ m: **(a)** GBM, **(b)** NCDE-based FBM, **(c)** DE-based FBM, and **(d)** difference between **(b)** and **(c)**.

derivative-free efficient optimization algorithm which can converge the excellent solution selected in each valley to the local extremum accurately and deterministically through “Reflection”, “Expansion”, “Contraction”, and “Shrinkage” operations of the simplex. By this cascading manner, a coarse search can be conducted in the first step namely the NCDE algorithm. Table 1 presents the core steps of the three-step multimodal optimization method based on the NCDE algorithm for processing an individual super-gather.

3. Parameter testing

In the three-step multimodal optimization method, the NCDE algorithm is used to ensure that there is at least one solution in each valley. The principle and implementation of the NCDE algorithm are simple. Only three custom parameters, namely population size, maximum number of iterations, and neighborhood size m, must be predefined. Population size and maximum number of iterations are the two core parameters that directly and jointly determine the computational cost. Neighborhood size m is not a sensitive parameter according to Qu et al. (2012) and Gao et al. (2022). Thus, we only need to test different combinations of the population size and maximum number of iterations for the NCDE algorithm on the super-gather.

For 2D super-gather and 3D conventional gather, the calculations are equivalent. Because the setting criteria of the two parameters for the 3D conventional gather and the related error analysis have been provided by Gao et al. (2022), we only test different combinations of the two parameters on the 3D super-gather. Based on the idea of the three-step multimodal optimization method, we do not conduct an error analysis for the 3D super-gather. Following Gao et al. (2022), for the 2D super-gather, when both the population size and the maximum number of iterations are set to 25, the NCDE algorithm can ensure that at least one individual moves into each valley.

For the 3D super-gather, we synthesize a seismic record of three intersecting events with different source and receiver slope orientations. These events consist of ricker wavelets with a dominant frequency of 30 Hz. The sampling number of the record is 601 with a sampling interval of 2 ms. The slope orientations are respectively (−0.30 s/km, 0.05 s/km, −0.10 s/km, −0.10 s/km), (0.20 s/km, −0.10 s/km, 0.20 s/km, −0.30 s/km), and (−0.10 s/km, 0.20 s/km, 0.30 s/km, 0.30 s/km). For each coordinate direction of

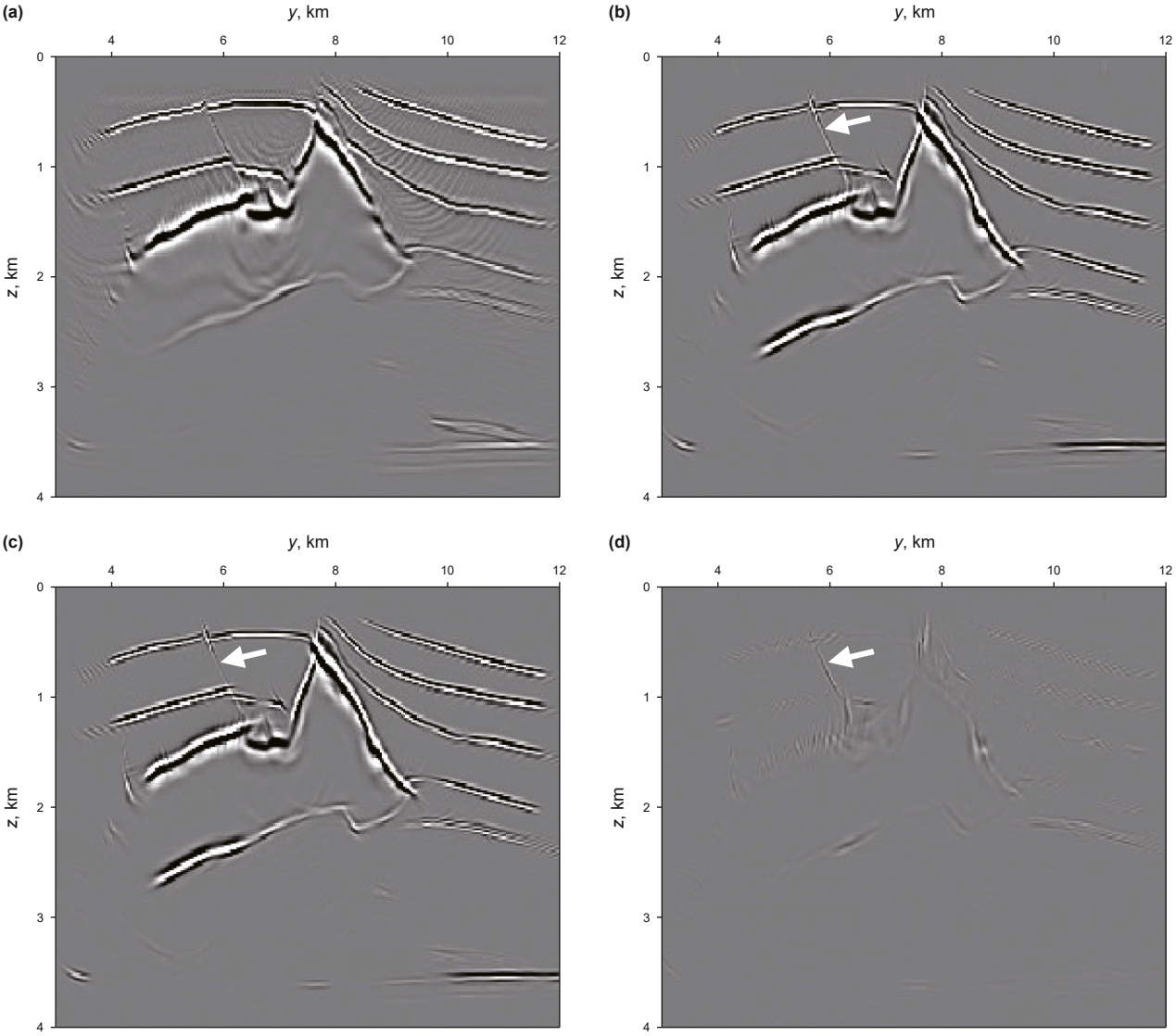

Fig. 13. Migration results of the 3D SEG/EAGE salt model at $x = 4620$ m: **(a)** GBM, **(b)** NCDE-based FBM, **(c)** DE-based FBM, and **(d)** difference between (b) and (c).

both source and receiver, the spatial sampling number is 5 with a sampling interval of 50 m, and the events intersect at the reference points of the super-gather at time 0.3 s. According to the strategy of Gao et al. (2022), we set a range for both parameters to select a suitable combination. The range of the population size is 100–140 with an interval of 5 and the range of the maximum number of iterations is 45–85 with an interval of 5.

Fig. 6 shows the results of 100 independent runs for each combination, indicating the count for the condition in which at least one individual moves into each valley. According to the theory of the NCDE algorithm, the number of function calls is equal to the population size multiplied by the maximum number of iterations. Thus, according to the statistical results, a population size of 130 and maximum number of iterations of 65 are considered suitable for the 3D super-gather. For the three-step multimodal optimization method, the number of function calls in the other two steps is relatively small, generally no more than 1000 in the case of 3D super-gather. Therefore, in general, the three-step multimodal optimization method based on the NCDE algorithm is an efficient algorithm that can overcome the high-dimensional computing problem while obtaining the source and receiver slope orientations of intersecting events.

4. Synthetic data tests

We first test the proposed method on the Marmousi 2 and 3D SEG/EAGE salt models to examine its applicability to complex wavefields. To evaluate its performance, the NCDE algorithm is replaced with the DE algorithm in the first step of the three-step multimodal optimization algorithm as a reference. For convenience, we refer to the FBM implementation using the NCDE algorithm as NCDE-based FBM and that using the DE algorithm as DE-based FBM. According to our experience, complex subsurface structures can be imaged well when at most three intersecting events are considered. Therefore, for the NCDE-based FBM, we consider three intersecting events at most, consistent with the parameter test above. In addition, all examples provided in this study are performed on a computing cluster consisting of four nodes. Each node contains an Intel Xeon 9242 processor (2.3 GHz

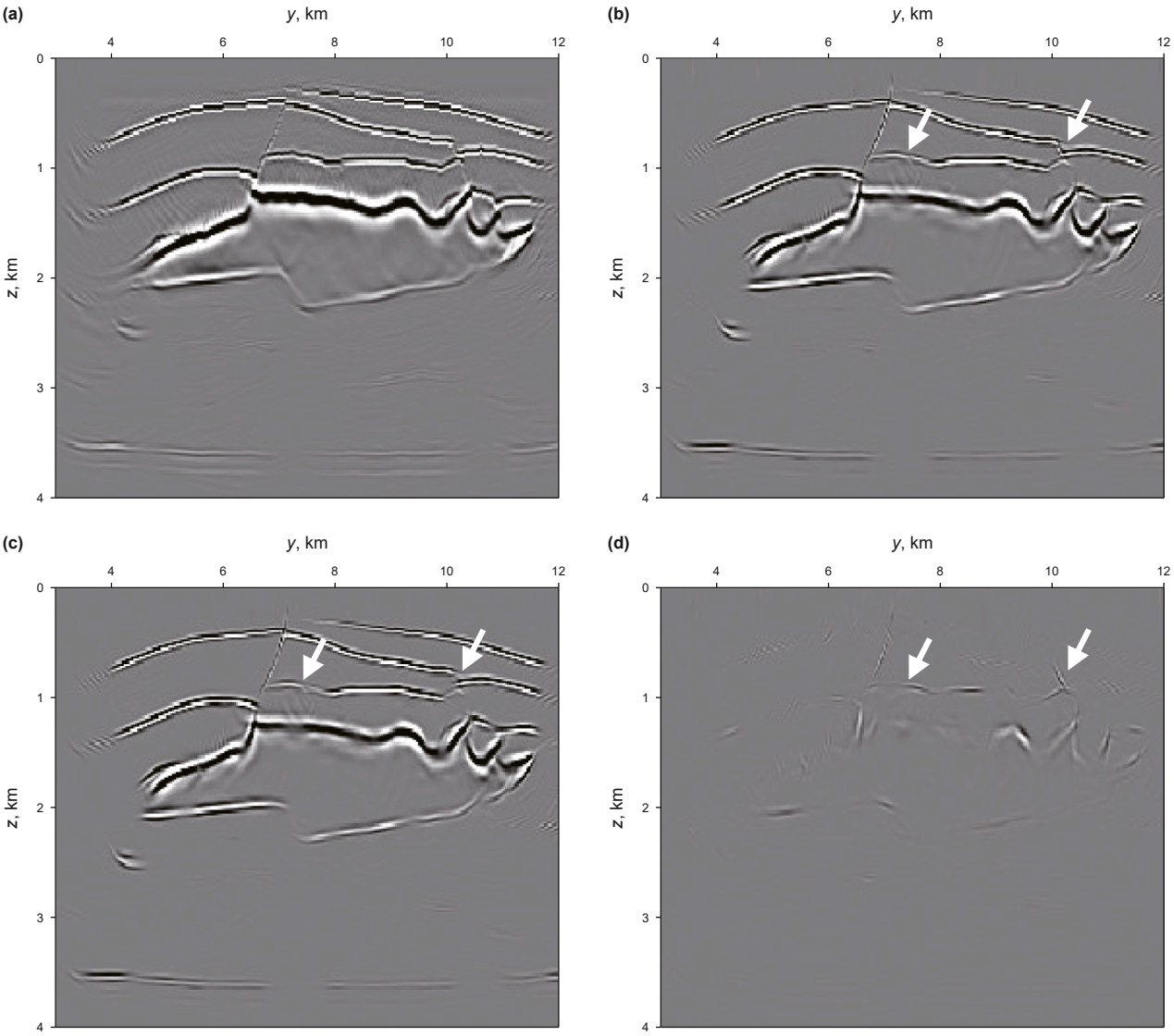

Fig. 14. Migration results of the 3D SEG/EAGE salt model at $x = 6260$ m: **(a)** GBM, **(b)** NCDE-based FBM, **(c)** DE-based FBM, and **(d)** difference between (b) and (c).

with 96 parallelizable threads), and all 384 threads are run concurrently.

4.1. Marmousi 2 model

The velocity profile of the Marmousi 2 model is illustrated in Fig. 7. The upper part of the model is covered by a seawater layer with a velocity of 1500 m/s, and the lower part consists of approximately 160 layers of strata with strong horizontal and vertical velocity changes; complex fault structures and an unconformity are existed in the model (Martin et al., 2006). The velocity profile is composed of 2400 horizontal grid points and 690 vertical grid points with a sampling interval of 5 m. Because the open version of the Marmousi 2 synthetic records contains multiple waves, we re-simulate a set of synthetic records using the absorbing boundary condition based on the P-wave velocity model. There are 461 shot gathers in the dataset with a source interval of 25 m distributed from 0.3 to 11.8 km. The source function is a Ricker wavelet with a dominant frequency of 20 Hz. The time length of the records is 6.8 s with a sampling interval of 4 ms. The maximum offset is limited to 7000 m with a trace interval of 10 m.

Fig. 8 shows the migration results of the Marmousi 2 model, where Fig. 8(a)–(c) display the results of GBM, NCDE-based FBM when at most three intersecting events are considered, and DE-based FBM, respectively. The result of NCDE-based FBM (Fig. 8(b)) show that the structures of the Marmousi 2 model are well-imaged with only some minor structures missing, which is very close to the result of GBM (Fig. 8(a)). However, compared with Fig. 8(b), some key structures are lost in Fig. 8(c), particularly in the areas of faults and steep-angle structures. Fig. 8(d) shows the difference between Fig. 8(b) and (c), from which we can see that the intersecting events mainly affect the migration results of faults and steep-angle structures.

Fig. 9 presents magnified views of the migration results of the Marmousi 2 model, where Fig. 9(a)–(d) show the results of NCDE-based FBM and Fig. 9(e)–(h) show those of DE-based FBM. When NCDE-based FBM is conducted, that is, considering at most three intersecting events, these complex subsurface structures (faults, unconformities and steep-angle structures) are better imaged.

Fig. 10 shows the angle-domain common image gathers (ADCIGs) extracted at $x = 10.3$ km for the Marmousi 2 model, where Fig. 10(a)–(c) display the results of GBM, NCDE-based FBM,

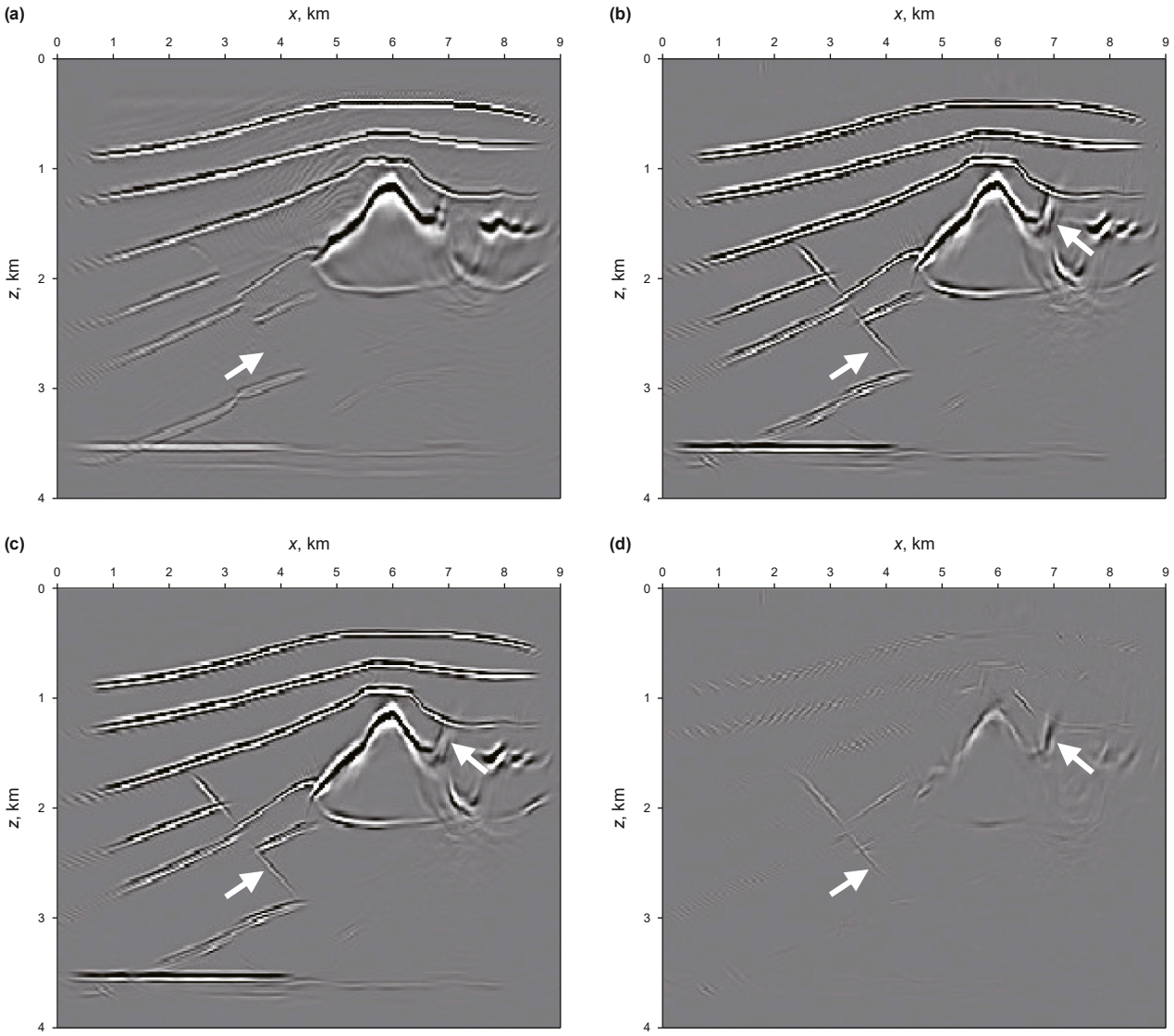

Fig. 15. Migration results of the 3D SEG/EAGE salt model at $y = 6280$ m: **(a)** GBM, **(b)** NCDE-based FBM, **(c)** DE-based FBM, and **(d)** difference between (b) and (c).

and DE-based FBM, respectively. The quality of the ADCIG obtained using NCDE-based FBM (Fig. 10(b)) is comparable to that of GBM (Fig. 10(a)). By comparing Fig. 10(b) with Fig. 10(c) (indicated by the white arrow), we find that neglecting intersecting events in FBM may result in the partial loss of some events in the ADCIG. Thus, the consideration of intersecting events is essential for FBM.

Table 2 presents the running times of NCDE-based FBM and GBM for the Marmousi 2 model. For velocity model building, the migration process is performed iteratively. Because the beam-forming step is velocity-independent, it only needs to be performed once. Thus, we also record the running time of the latter two steps (beam propagation and image forming) of NCDE-based FBM. NCDE-based FBM exhibits extremely high computational efficiency compared with GBM, which means that NCDE-based FBM is suitable for velocity model building, even for complex subsurface structures.

4.2. 3D SEG/EAGE salt model

The original grid size of the 3D SEG/EAGE salt model is 676 × 676× 210 in the x, y, and z directions, with a spacing interval of 20 m in each direction (Aminzadeh, 1996). However, the acquisition geometry covers only part of the model. Thus, we select only the covered portion for the migration test. The size of the migration portion is 481 × 451× 210, for which the range in x-direction is from 0 km to 9 km and that in y-direction is from 3 to 12 km. The interval between the original shot lines is 160 m, which is slightly large for estimating the corresponding slope orientation. Therefore, based on the original acquisition geometry, we double the density of the shot lines and re-simulate the records. A Ricker wavelet with a dominant frequency of 15 Hz is used as the source function. The time length of the records is 4.92 s with a sampling interval of 4 ms. Considering the typical structures of the salt model such as faults and high-velocity salt body, four representative velocity profiles at $z = 1020$ m, $x = 4620$ m, $x = 6260$ m, and $y = 6280$ m are selected for display (Fig. 11).

Fig. 12 illustrates the migration results of the 3D SEG/EAGE salt model at $z = 1020$ m. Fig. 12(a)–(c) show the results of GBM, NCDE-based FBM when at most three intersecting events are considered, and DE-based FBM, respectively. Fig. 12(d) presents the difference between Fig. 12(b) and (c). For the result of GBM in Fig. 12(a), there are severe migration artifacts, whereas few artifacts are apparent in the results of NCDE-based FBM and DE-based FBM. This is

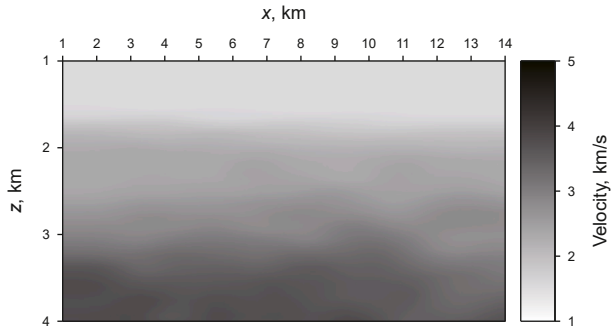

Fig. 17. Velocity profile of the 2D offshore seismic dataset.

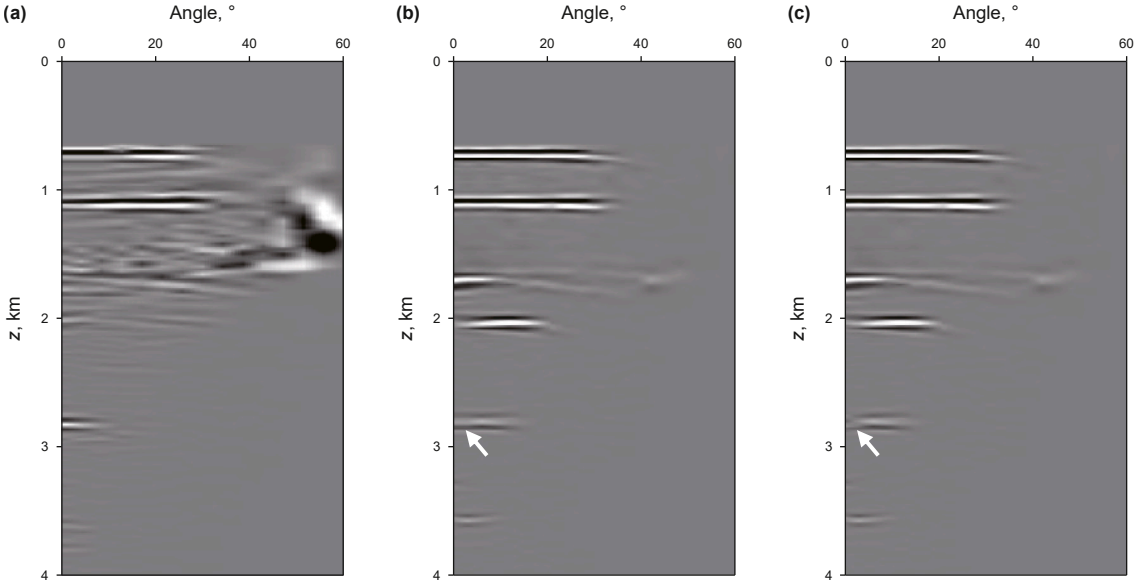

Fig. 16. ADCIGs of 3D SEG/EAGE salt model extracted at (3.6 km, 7 km): **(a)** GBM, **(b)** NCDE-based FBM when at most three intersecting events are considered, and **(c)** DE-based FBM.

Table 3
Comparison of the running times of NCDE-based FBM and GBM for the 3D SEG/EAGE salt model.

Migration methods	Running time, h
NCDE-based FBM	12.74
NCDE-based FBM (just record the beam-propagation and image-forming steps)	0.32
GBM	328.94

because the fold of the acquisition geometry is not very high, and GBM acts like a Kirchhoff migration, spreading the energy over a full ellipsoid surface. FBM spreads energy over a beam patch and the migration aperture is limited. DE-based FBM can only consider the slope orientation of the most coherent event when events intersect. Compared with Fig. 12(b), some key structures are missing in the areas of faults and salt boundary in Fig. 12(c). Fig. 12(d) shows that the intersecting events mainly contribute to the imaging results of faults and salt boundary.

Fig. 13 shows the migration results of the 3D SEG/EAGE salt model at $x = 4620$ m. Fig. 13(a)–(c) are the results of GBM, NCDE-based FBM when at most three intersecting events are considered,

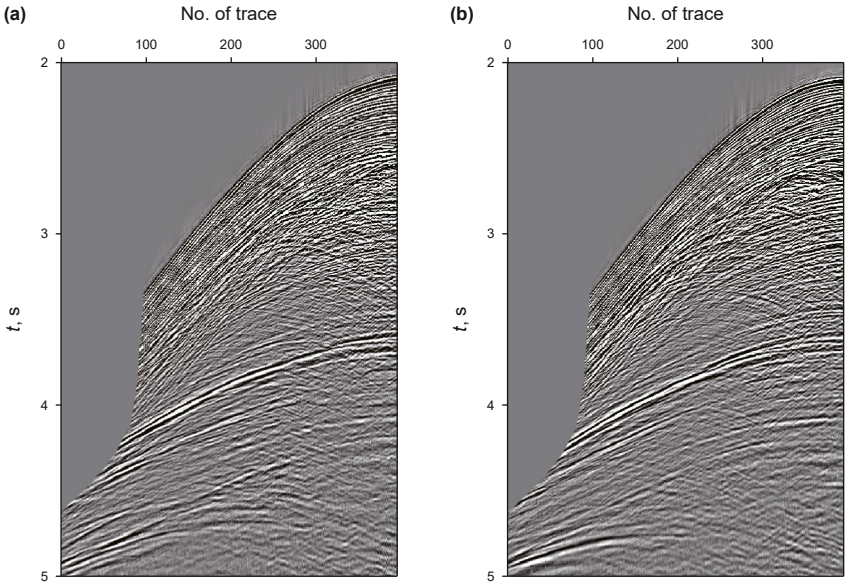

Fig. 18. Two common shot gathers extracted from the 2D offshore seismic dataset.

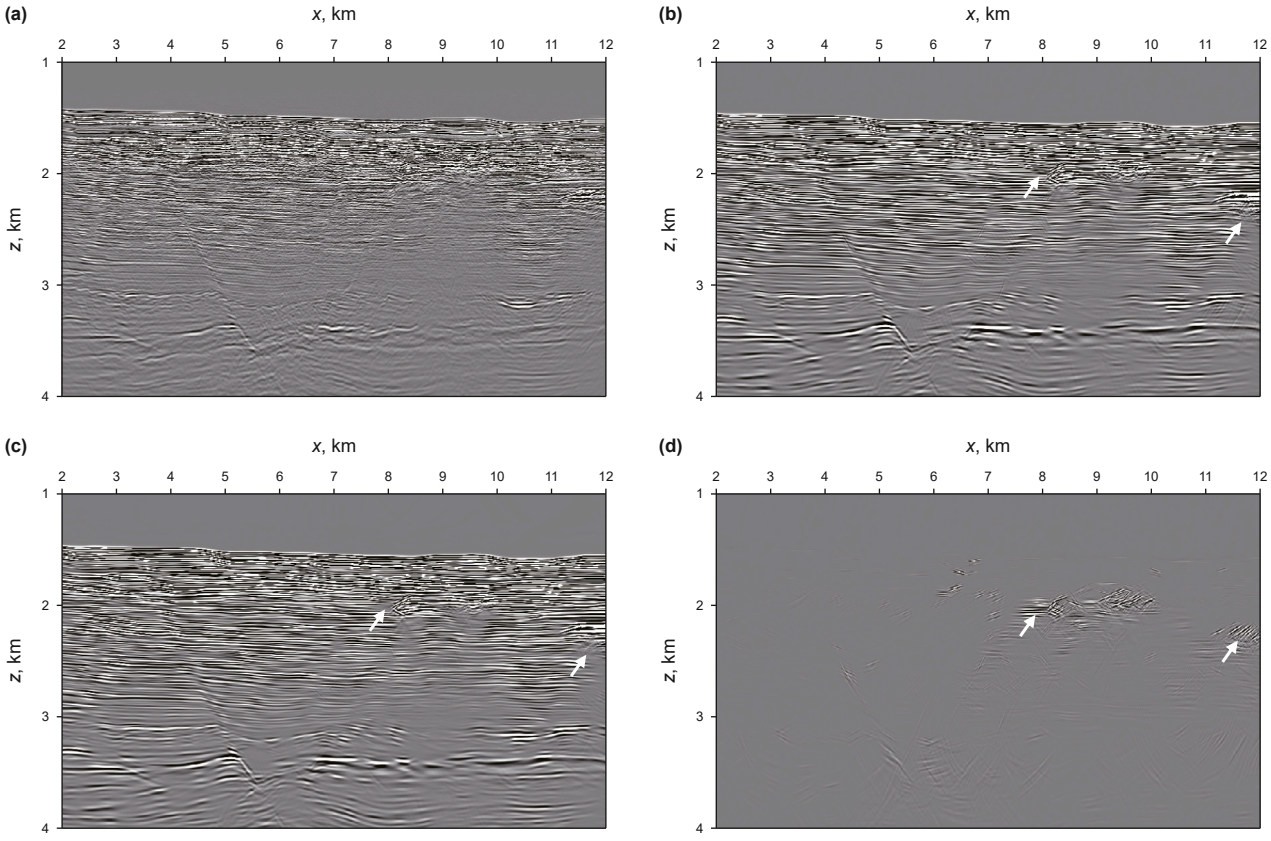

Fig. 19. Migration results of the 2D offshore seismic dataset: **(a)** GBM, **(b)** NCDE-based FBM when at most three intersecting events are considered, **(c)** DE-based FBM, and **(d)** difference between (b) and (c).

and DE-based FBM, respectively. Fig. 13(d) shows the difference between Fig. 13(b) and (c). Similarly, obvious migration artifacts appear in the result of GBM (Fig. 13(a)). The imaging result of the overall structure in Fig. 13(b) is close to that in Fig. 13(a). In Fig. 13(c), part of the important fault is missing (indicated by the white arrow). Fig. 13(d) illustrates the importance of considering intersecting events for accurate imaging of faults and salt boundary.

Fig. 14 shows the migration results of the 3D SEG/EAGE salt model at $x = 6260$ m. Fig. 14(a)–(c) show the results of GBM, NCDE-based FBM when at most three intersecting events are considered, and DE-based FBM, respectively. Fig. 14(d) shows the difference between Fig. 14(b) and (c). The imaging effect of the results is similar to those of the two profiles above. The imaging result of the subsurface structure for NCDE-based FBM is close to that for GBM and some important structures are missing in the imaging result of DE-based FBM.

Fig. 15 displays the migration results of the 3D SEG/EAGE salt model at $y = 6280$ m. Fig. 15(a)–(c) are the results of GBM, NCDE-based FBM when at most three intersecting events are considered, and DE-based FBM, respectively. Fig. 15(d) shows the difference between Fig. 15(b) and (c). Surprisingly, the fault in the left part of the model disappears from the imaging result of GBM. In the results of NCDE-based and DE-base FBM, the fault can be clearly observed. We believe that owing to the low fold of this dataset, the migration swings of GBM cause this result. In addition, by comparing the result of NCDE-based FBM with that of DE-based FBM, the contribution of intersecting events for imaging faults and salt boundary is apparent.

Fig. 16 shows the ADCIGs extracted at (3.6 km, 7 km) for the 3D SEG/EAGE salt model, where Fig. 16(a)–(c) present the results of GBM, NCDE-based FBM when at most three intersecting events are considered, and DE-based FBM, respectively. We can see that owing to the low-fold problem, migration noise is enhanced for GBM. The results of FBM show reduced migration artifacts. A comparison of the result in Fig. 16(b) with that in Fig. 16(c) shows that, the DE-based FBM may lose energy for certain events. This suggests that the ADCIGs generated from the NCDE-based FBM are preferred for velocity model building.

Table 3 lists the running times of NCDE-based FBM and GBM for the 3D SEG/EAGE salt model. The result shows that in the case of velocity model building for 3D condition, NCDE-based FBM can improve the efficiency by more than two orders of magnitude compared to GBM, while obtaining close imaging results for complex subsurface structures.

5. Application to offshore seismic data

We use a 2D offshore seismic dataset to test the practicality of the NCDE-based FBM. The velocity model is composed of 2800 horizontal grid points and 600 vertical grid points, with a horizontal sampling interval of 5 m and a vertical sampling interval of 6.25 m (Fig. 17). There are 501 shot gathers in the dataset with a

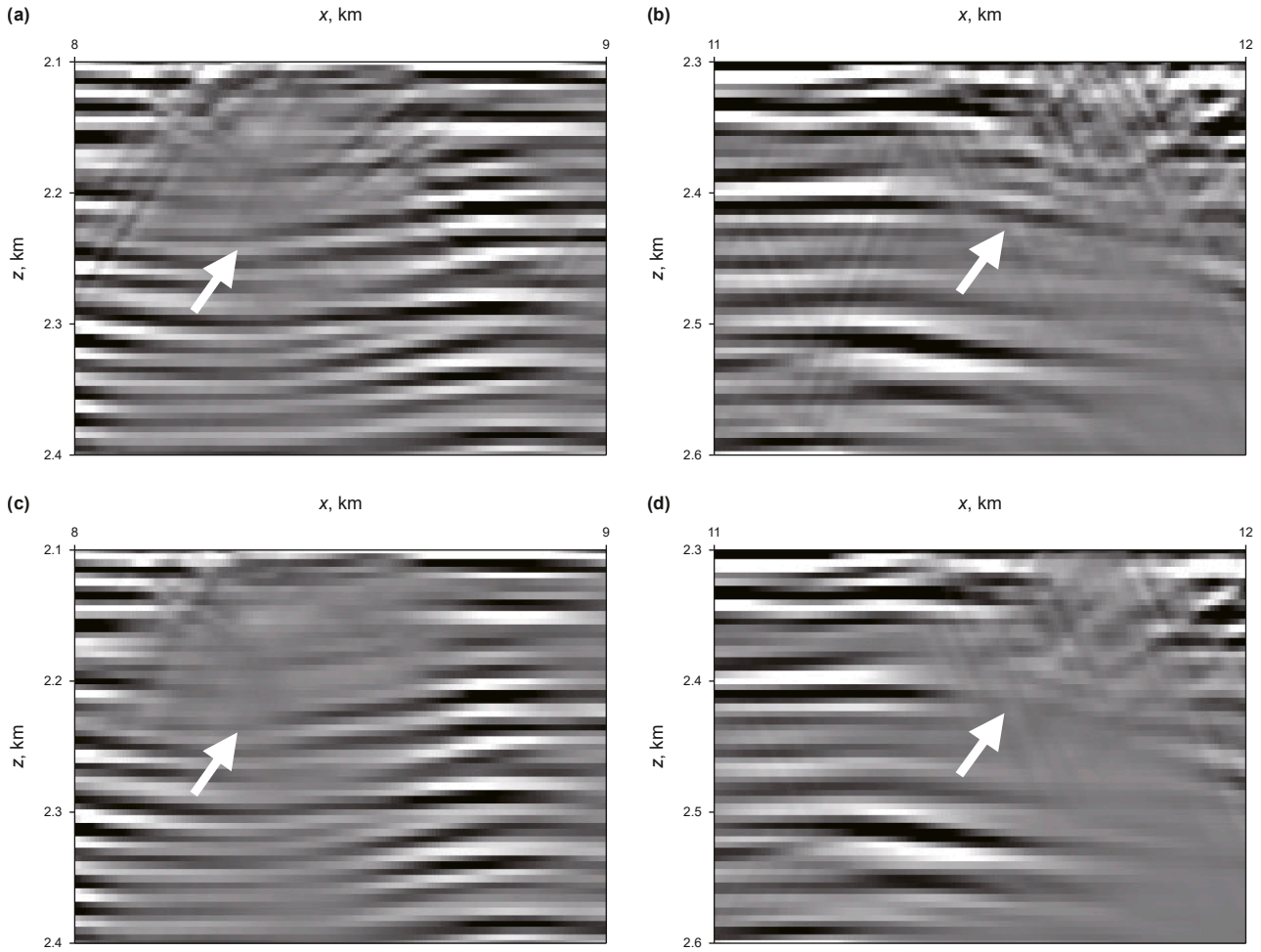

Fig. 20. Magnified views of the migration results of the 2D offshore seismic dataset: **(a)** and **(b)** are for result of NCDE-base FBM, and **(c)** and **(d)** are for that of DE-based FBM.

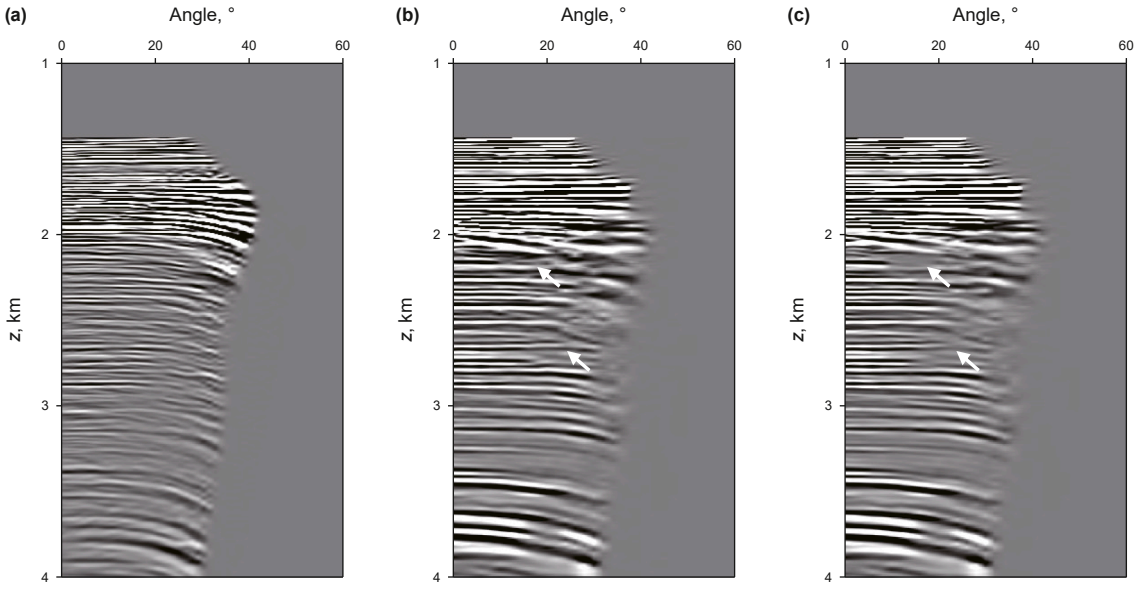

Fig. 21. ADCIGs of the 2D offshore seismic dataset at $x = 9.68$ km: **(a)** GBM, **(b)** NCDE-based FBM when at most three intersecting events are considered, **(c)** DE-based FBM.

Table 4
Comparison of the running times of NCDE-based FBM and GBM for the 2D offshore seismic dataset.

Migration methods	Running time, min
NCDE-based FBM	10.24
NCDE-based FBM (just record the beam-propagation and image-forming steps)	3.26
GBM	104.84

source interval of 25 m distributed from 2.162 km to 14.662 km. The time length of the records is 5 s with a sampling interval of 4 ms. The maximum offset is limited to 5.16 km with a trace interval of 12.5 m. Fig. 18 shows two common shot gathers extracted from this offshore seismic dataset. We can observe that the phenomena in which events intersect are well-developed.

Fig. 19 shows the migration results of the 2D offshore seismic dataset, where Fig. 19(a)–(c) show the migration results of GBM, NCDE-based FBM when at most three intersecting events are considered, and DE-based FBM, respectively. Fig. 19(d) shows the difference between Fig. 19(b) and (c). The structures in the imaging results of GBM and NCDE-based FBM are basically consistent. The result of GBM shows higher fidelity than the result of NCDE-based FBM, whereas the results of FBM exhibit higher signal-to-noise ratio and more continuous events. This is because the conventional GBM follows the dynamic principle of wave propagation, whereas FBM mainly focuses on structural imaging. The beams in FBM are formed by stacking along the respective slope orientations, which has the effect of suppressing random noise. And the migration aperture of FBM is limited by the beam patch. By comparing Fig. 19(b) with Fig. 19(c), we can see that some structures are missing from the results of the DE-based FBM. Magnified views of the results of NCDE-based FBM and DE-based FBM (Fig. 20) highlight these features.

Fig. 21 shows the ADCIGs extracted at $x = 9.68$ km for the 2D offshore seismic dataset, where Fig. 21(a)–(c) display the results of GBM, NCDE-based FBM when at most three intersecting events are considered, and DE-based FBM, respectively. The results of GBM and NCDE-based FBM are comparable, whereas for DE-based FBM, the continuity of certain events is poor (indicated by the white arrows). Therefore, both the imaging profile and the ADCIG for NCDE-based FBM produce satisfactory results for the 2D offshore dataset, which demonstrates its practicality.

Table 4 lists the running times of NCDE-based FBM and GBM for the 2D offshore seismic dataset. We can observe that an excellent computational performance similar to that of the Marmousi 2 model is achieved by NCDE-based FBM, which is an order of magnitude faster than that of GBM.

6. Conclusions

We have developed an FBM method and propose a new implementation that can handle intersecting events that have a significant impact on the imaging of complex subsurface structures. The new implementation is accomplished by applying a three-step multimodal optimization method based on the NCDE algorithm to the beam-forming step to estimate the source and receiver slope orientation of the beam quickly and accurately. For the 2D super-gather, when the population size and maximum number of iterations are set to 25, the NCDE algorithm can ensure that at least one individual moves into each valley. For the 3D super-gather, the criteria for these two parameters are 130 and 65, respectively. The latter two steps, hill-valley detection algorithm and Nelder-Mead simplex algorithm, are not algorithms that need heavy computational cost. Thus, the three-step multimodal optimization method can overcome the high-dimensional computing problem while obtaining source and receiver slope orientations of intersecting events in the super-gather. The applications to the Marmousi 2 and 3D SEG/EAGE salt models both verify the capability of the proposed implementation of FBM for dealing with intersecting events. The application to a 2D offshore seismic dataset with abundant intersecting events validates its practicality. The running times of the proposed implementation of FBM for all cases also verify its high efficiency. The new implementation of FBM can achieve an imaging quality close to that of GBM for complex subsurface structures, and in some special cases, even

better. High-quality ADCIGs is produced in all cases. Therefore, the new implementation of FBM can be regarded as a fast and accurate migration method that is particularly suitable for velocity model building.

CRediT authorship contribution statement

Zhi-Miao Chang: Writing – review & editing, Writing – original draft, Visualization, Software, Methodology, Investigation, Formal analysis, Data curation, Conceptualization. **Fu-Xing Han:** Writing – review & editing, Supervision, Resources, Project administration. **Zheng-Hui Gao:** Writing – review & editing, Writing – original draft, Visualization, Supervision, Software, Resources, Project administration, Methodology, Funding acquisition. **Zhang-Qing Sun:** Writing – review & editing. **Shou-Dong Huo:** Writing – review & editing, Supervision, Investigation. **Gang Li:** Writing – review & editing. **Ming Zhang:** Writing – review & editing.

Declaration of competing interest

The authors declare that they have no known competing financial interests or personal relationships that could have appeared to influence the work reported in this paper.

Acknowledgments

We thank the Natural Science Foundation of China (42304128 and 42074150), the National Key Research and Development Program of China (2023YFC2906704-5 and 2023YFC370790), the Mount Tai Industry Leading Talent Project Special Fund Support (tscx202312018), the Jinan Science and Technology Innovation Development Plan (Social Livelihood Special Project) (202131001).

References

Aminzadeh, F., 1996. 3-D Salt and Overthrust Seismic Models. American Association of Petroleum Geologists. https://doi.org/10.1306/St42605C29.

Chopra, S., Marfurt, K.J., 2007. Seismic Attributes for Prospect Identification and Reservoir Characterization. Society of Exploration Geophysicists. https://doi.org/10.1190/1.9781560801900.ch3.

Das, S., Maity, S., Qu, B.Y., Suganthan, P.N., 2011. Real-parameter evolutionary multimodal optimization—A survey of the state-of-the-art. Swarm Evol. Comput. 1 (2), 71–88. https://doi.org/10.1016/j.swevo.2011.05.005.

Esmersoy, C., Hawthorn, A., Durrand, C., Armstrong, P., 2005. Seismic MWD: Drilling in time, on time, it's about time. Lead. Edge 24 (1), 56–62. https://doi.org/10.1190/1.1859702.

Fomel, S., Tanushev, N., 2009. Time-domain seismic imaging using beams. In: 79th Annual International Meeting. SEG Expanded Abstracts, pp. 2747–2752. https://doi.org/10.1190/1.3255419.

Fomel, S., 2002. Applications of plane-wave destruction filters. Geophysics 67 (6), 1946–1960. https://doi.org/10.1190/1.1527095.

Gao, F.C., Zhang, P., 2007. Fast beam migration based interactive seismic imaging. Geophys. Prospect. Pet. 46 (6), 626–629 (in Chinese).

Gao, F.C., Zhang, P., Wang, B., Dirks, V., 2006. Fast beam migration – a step toward interactive imaging. In: 76th Annual International Meeting, SEG Expanded Abstracts, pp. 2470–2474. https://doi.org/10.1190/1.2370032.

Gao, Z.H., Han, F.X., Sun, Z.Q., Yu, P., Xiong, D., Liu, Z., Hou, S.D., 2022. Simultaneous estimation of local intersecting slopes. Geophysics 87 (4), V293–V305. https://doi.org/10.1190/geo2021-0460.1.

Gao, Z.H., Huo, S.D., Liang, Y., Huang, L., Shu, G., Wei, Y., 2019. Simultaneous estimation of local intersecting slopes by a multimodal optimization method. In: 81st EAGE Conference and Exhibition, pp. 1–5. https://doi.org/10.3997/2214-4609.201901482.

Hill, N.R., 1990. Gaussian beam migration. Geophysics 55 (11), 1416–1428. https://doi.org/10.1190/1.1442788.

Hill, N.R., 2001. Prestack Gaussian-beam depth migration. Geophysics 66 (4), 1240–1250. https://doi.org/10.1190/1.1487071.

Holland, J.H., 1992. Genetic algorithms. Sci. Am. 267 (1), 66–73. https://doi.org/10.1038/scientificamerican0792-66.

Hu, H., Liu, Y.K., Osen, A., Zheng, Y.C., 2015. Compression of local slant stacks by the estimation of multiple local slopes and the matching pursuit decomposition. Geophysics 80 (6), WD175–WD187. https://doi.org/10.1190/geo2014-0595.1.

Hua, B., McMechan, G.A., 2003. Parsimonious 2D prestack Kirchhoff depth migration. Geophysics 68 (3), 1043–1051. https://doi.org/10.1190/1.1581075.

Hua, B., McMechan, G.A., 2009. Parsimonious 3D prestack Kirchhoff depth migration. J. Seismic Explor. 18 (2), 157–179.

Huo, S, Zhu, W, Shi, T, 2017. Iterative dip-steering median filter. J. Appl. Geophys. 144, 151–156.

Kennedy, J., Eberhart, R., 1995. Particle swarm optimization. In: Proceedings of ICNN'95 International Conference on Neural Networks, pp. 1942–1948. https://doi.org/10.1109/ICNN.1995.488968.

Leveille, J.P., Jones, L.F., Zhou, Z.Z., Wang, B., Liu, F.Q., 2011. Subsalt imaging for exploration, production, and development: A review. Geophysics 76 (5), WB3–WB20. https://doi.org/10.1190/geo2011-0156.1.

Martin, G.S., Wiley, R., Marfurt, K.J., 2006. Marmousi 2: An elastic upgrade for Marmousi. Lead. Edge 25 (2), 156–166. https://doi.org/10.1190/1.2172306.

Masters, R., Sherwood, K., 2005. Beam pre-stack depth migration algorithm in a 3D PSDM non-exclusive reprocessing project, Sergipe-Alagoas Basin. In: 9th International Congress of the Brazilian Geophysical Society & EXPOGEF, pp. 1527–1529. https://doi.org/10.1190/sbgf2005-304.

Nelder, J.A., Mead, R., 1965. A simplex method for function minimization. Comput. J. 7 (4), 308–313. https://doi.org/10.1093/comjnl/7.4.308.

Popovici, A.M., Tanushev, N., Sturzu, I., Musat, I., Tsingas, C., Fomel, S., 2013a. Fast beam migration using plane wave destructor (PWD) beam forming. In: SPE Middle East Oil and Gas Show and Conference. https://doi.org/10.2118/164259-MS.

Popovici, A.M., Tanushev, N., Sturzu, I., Musat, I., Tsingas, C., Fomel, S., 2013b. Fast beam migration using plane wave destructor (PWD) beam forming. In: 75th EAGE Conference & Exhibition Incorporating SPE EUROPEC. https://doi.org/10.3997/2214-4609.20130725.

Price, K., Storn, R.M., Lampinen, J.A., 2006. Differential Evolution: A Practical Approach to Global Optimization. Springer Science and Business Media. https://doi.org/10.1007/3-540-31306-0.

Qu, B.Y., Suganthan, P.N., Liang, J.J., 2012. Differential evolution with neighborhood mutation for multimodal optimization. IEEE Trans. Evol. Comput. 16 (5), 601–614. https://doi.org/10.1109/TEVC.2011.2161873.

Sherwood, J.W.C., Sherwood, K., Tieman, H., Schleicher, K., 2008. 3D beam prestack depth migration with examples from around the world. In: 78th Annual International Meeting, SEG Expanded Abstracts, pp. 438–442. https://doi.org/10.1190/1.3054840.

Sherwood, J.W.C., Sherwood, K., Tieman, H., Schleicher, K., 2009. 3D beam prestack depth migration with examples from around the world. Lead. Edge 28 (9), 1120–1127. https://doi.org/10.1190/1.3236382.

Su, Q., Zeng, H.H., Tian, Y.C., Li, H.L., Lyu, L., Zhang, X.M., 2021. High-resolution seismic processing technique with broadband, wide-azimuth, and high-density seismic data—A case study of thin-sand reservoirs in eastern China. Interpretation 9 (3), T833–T842. https://doi.org/10.1190/INT-2020-0107.1.

Sun, H., Schuster, G.T., 2001. 2-D wavepath migration. Geophysics 66 (5), 1528–1537. https://doi.org/10.1190/1.1487099.

Sun, Y.H., Qin, F.H., Checkles, S., Leveille, J.P., 2000a. 3-D prestack Kirchhoff beam migration for depth imaging. Geophysics 65 (5), 1592–1603. https://doi.org/10.1190/1.1444847.

Sun, Y.H., Qin, F.H., Checkles, S., Leveille, J.P., 2000b. A beam approach to Kirchhoff depth imaging. Lead. Edge 19 (1), 1168–1173. https://doi.org/10.1190/1.1438496.

Tanushev, N., Popovici, A.M., Hardesty, S., 2017. Fast, high-resolution beam tomography and velocity-model building. Lead. Edge 36 (2), 140–145. https://doi.org/10.1190/tle36020140.1.

Ursem, R.K., 1999. Multinational evolutionary algorithms. In: Proceedings of the 1999 Congress on Evolutionary Computation, 3, pp. 1633–1640. https://doi.org/10.1109/CEC.1999.785470.

Wang, B., Ji, J., Mason, C., Gajawada, S., Kim, Y., 2008. Beam-based interactive imaging for salt interpretation and salt model building. In: 78th Annual International Meeting, SEG Expanded Abstracts, pp. 3073–3077. https://doi.org/10.1190/1.3063983.

Wang, H.Z., 2019. Key problem analysis in seismic exploration based on wide-azimuth, high-density, and broadband seismic data. Geophys. Prospect. Pet. 58 (3), 313–324. https://doi.org/10.3969/j.issn.1000-1441.2019.03.001 (in Chinese).

Wu, X.M., Fomel, S., Hudec, M., 2018. Fast salt boundary interpretation with optimal path picking. Geophysics 83 (3), O45–O53. https://doi.org/10.1190/geo2017-0481.1.

Xie, Y., Gajewski, D., 2017. 5-D interpolation with wave-front attributes. Geophys. J. Int. 211 (2), 897–919. https://doi.org/10.1093/gji/ggx334.

Yang, S., Peng, C., 2018. Seismic guided drilling: A technology to reduce drilling risk and increase drilling success rate. Geophys. Prospect. Pet. 57 (4), 627–636. https://doi.org/10.3969/j.issn.1000-1441.2018.04.018 (in Chinese).

Zhang, Y., 2018. From imaging to inversion: Theory, practice, and technological evolution of prestack depth migration. Geophys. Prospect. Pet. 57 (1), 1–23. https://doi.org/10.3969/j.issn.1000-1441.2018.01.001 (in Chinese).